

RESEARCH ARTICLE

10.1002/2016JD025823

Key Points:

- Evaluation of MERRA-2 atmospheric temperature, ozone, and water vapor profiles in the midlatitudes, Arctic, and tropics
- Radiation closure study: calculate clear-sky radiative fluxes using hybrid and MERRA-2 profiles with observational constraints
- Generation of hybrid atmospheric profiles from collocated MLS and DOE ARM-merged soundings used for the evaluation

Correspondence to:

X. Dong,
xdong@email.arizona.edu

Citation:

Dolinar, E. K., X. Dong, B. Xi, J. H. Jiang, and N. G. Loeb (2016), A clear-sky radiation closure study using a one-dimensional radiative transfer model and collocated satellite-surface-reanalysis data sets, *J. Geophys. Res. Atmos.*, 121, 13,698–13,714, doi:10.1002/2016JD025823.

Received 22 AUG 2016

Accepted 2 NOV 2016

Accepted article online 7 NOV 2016

Published online 25 NOV 2016

A clear-sky radiation closure study using a one-dimensional radiative transfer model and collocated satellite-surface-reanalysis data sets

Erica K. Dolinar¹, Xiquan Dong², Baike Xi¹, Jonathan H. Jiang³, and Norman G. Loeb⁴
¹Department of Atmospheric Sciences, University of North Dakota, Grand Forks, North Dakota, USA, ²Department of Hydrology and Atmospheric Sciences, University of Arizona, Tucson, Arizona, USA, ³Jet Propulsion Laboratory, Pasadena, California, USA, ⁴NASA Langley Research Center, Hampton, Virginia, USA

Abstract Earth's climate is largely determined by the planet's energy budget, i.e., the balance of incoming and outgoing radiation at the surface and top of atmosphere (TOA). Studies have shown that computing clear-sky radiative fluxes are strongly dependent on atmospheric state variables, such as temperature and water vapor profiles, while the all-sky fluxes are greatly influenced by the presence of clouds. NASA-modeled vertical profiles of temperature and water vapor are used to derive the surface radiation budget from Clouds and Earth Radiant Energy System (CERES), which is regarded as one of the primary sources for evaluating climate change in climate models. In this study, we evaluate the Modern-Era Retrospective Analysis for Research and Applications version 2 (MERRA-2) reanalyzed clear-sky temperature and water vapor profiles with newly generated atmospheric profiles from Department of Energy Atmospheric Radiation Measurement (ARM)-merged soundings and Aura Microwave Limb Sounder retrievals at three ARM sites. The temperature profiles are well replicated in MERRA-2 at all three sites, whereas tropospheric water vapor is slightly dry below ~700 hPa. These profiles are then used to calculate clear-sky surface and TOA radiative fluxes from the Langley-modified Fu-Liou radiative transfer model (RTM). In order to achieve radiative closure at both the surface and TOA, the ARM-measured surface albedos and aerosol optical depths are adjusted to account for surface inhomogeneity. In general, most of the averaged RTM-calculated surface downward and TOA upward shortwave and longwave fluxes agree within ~5 W/m² of the observations, which is within the uncertainties of the ARM and CERES measurements. Yet still, further efforts are required to reduce the bias in calculated fluxes in coastal regions.

1. Introduction

Correctly estimating and tracking changes in the Earth's radiation budget is one of the top priorities for climate monitoring and prediction [Hartmann *et al.*, 1986; Trenberth *et al.*, 2009], with clouds, aerosols, and greenhouse gases having a significant impact on the radiation budget [Ramanathan, 1987; Kiehl and Trenberth, 1997]. Since clouds are highly variable in time and space, characterizing them in numerical weather prediction and climate models is quite challenging. Complex processes related to cloud microphysical properties, cloud-aerosol interactions, and cloud-radiation interactions are oftentimes simplified in order to facilitate the simulation process in the models [Dudek *et al.*, 1996; Khain *et al.*, 2000; Menon *et al.*, 2002].

Cloud radiative effects (CREs) are defined as the difference between the radiative flux in all-sky and clear-sky conditions [Ramanathan *et al.*, 1989]. While clouds and their CRE are poorly represented in climate models, the clear-sky components can be just as flawed [Allen, 2000; Wild *et al.*, 2006; Dolinar *et al.*, 2015; Stanfield *et al.*, 2015; Ruzmaikin *et al.*, 2015]. Better constraints and understanding of clear-sky radiative transfer is an ongoing and necessary effort. The primary goal of satellite projects such as the Clouds and Earth Radiant Energy System (CERES) [Wielicki *et al.*, 1996], the Global Energy and Water Cycle Experiment (GEWEX) Surface Radiation Budget (SRB) [Stackhouse *et al.*, 2011], and the International Satellite Cloud Climatology Project (ISCCP) [Zhang *et al.*, 2004] is to provide a global view of the interactions between clouds and radiation. These data sets are frequently used as evaluation tools for climate model simulations of clouds and top-of-atmosphere (TOA) radiation budgets [Pincus *et al.*, 2009; Dolinar *et al.*, 2015; Stanfield *et al.*, 2015; Wild *et al.*, 2015; Ruzmaikin *et al.*, 2015]. For CERES, surface radiation budgets are computed from coincident spectral imagers on Sun-synchronous (e.g., the Moderate Resolution Imaging Spectroradiometer (MODIS)) and geostationary platforms using a simplified one-dimensional radiative transfer model (RTM). While

inputs to the RTM calculations rely on various parameterizations, all can be tuned and constrained by the CERES-measured TOA fluxes. In ISCCP and GEWEX SRB, surface radiative fluxes are computed using either an RTM or a parameterized RTM. In each project, the derived surface radiative fluxes depend greatly on the input of atmospheric temperature and water vapor profiles. In CERES, pressure, temperature, and water vapor profiles are specified from Goddard Earth Observing System (GEOS) version 5.4.1 [Bloom *et al.*, 2005], a gridded reanalysis data product from the Goddard Modeling and Assimilation Office. In ISCCP and SRB, temperature and water vapor are retrieved directly from microwave sounders [Zhang *et al.*, 2004]. In a study by Moy *et al.* [2010] rapid RTM (RRTM)-computed clear-sky outgoing LW radiation (OLR) fluxes at the Atmospheric Radiation Measurement (ARM) Southern Great Plains (SGP) site were compared to observed fluxes from CERES. The RRTM OLR fluxes are accurate to 0.2 and 0.8% of CERES when coincident radiosonde and Atmospheric Infrared Sounder (AIRS) retrieved profiles are used, respectively. Additionally, Susskind *et al.* [2012] found that CERES and AIRS clear-sky OLR estimates correlate well, despite differences in retrieval algorithms, RTMs, and input data. Charlock and Alberta [1996] compared observed surface all-sky and clear-sky SW and LW fluxes to RTM-calculated fluxes at the ARM SGP site. Two types of input profiles are used to calculate the surface fluxes; each produce a different result but are biased in the same direction.

Understanding the sensitivity of the calculated surface radiative fluxes to atmospheric input profiles is a necessary prerequisite to developing global radiation data products. The characterization of clouds (e.g., cloud amount, cloud overlap, and microphysical properties) proves to be one of the largest sources of uncertainty in deriving surface fluxes. The ambiguity in calculating clear-sky fluxes is also worthwhile to investigate because it offers a foundation for scientists to understand the RTM's calculations without the inherent issues associated with clouds. The calculated surface clear-sky LW radiative flux is primarily determined by the atmospheric temperature and water vapor profiles and surface temperature, while the SW flux is mainly a function of the scattering and absorption of atmospheric molecules and aerosols and surface reflection. In this study, temperature and water vapor profiles from Modern-Era Retrospective Analysis for Research and Applications version 2 (MERRA-2), along with the climatic aerosol optical depths over the three ARM sites, are used as input to the radiative transfer model to calculate the clear-sky surface and TOA radiative fluxes.

The first objective of this study is to evaluate the MERRA-2 clear-sky temperature and water vapor profiles using a newly generated atmospheric profile data set. As a natural extension of the previously noted studies, the second objective is to analyze the differences between the RTM-calculated fluxes (with different atmospheric input profiles) and observations at the surface and TOA; this will provide a radiation closure study for the first objective. If the calculated surface and TOA fluxes match well with the observed fluxes under clear-sky conditions, then we will have confidence to investigate cloudy conditions and their radiative heating/cooling rates in the future.

Section 2 documents the ground- and satellite-based data sets used in this study, as well as several of the notable updates in the recently released MERRA-2 reanalysis. Section 3 presents our evaluation results for objectives 1 and 2. Section 4 revisits some of the major conclusions offered from this study.

2. Data and Methods

2.1. ARM Ground-Based Observations and Retrievals

Three ARM sites have been chosen for this study due not only to their different climate regimes but also to make use of the variety of available data at these locations. The top plot of Figure 1 shows the locations of the ARM SGP; the North Slope Alaska (NSA); and Tropical Western Pacific (TWP) Darwin, Australia (C3) sites, which effectively represent midlatitude continental, coastal polar, and coastal tropical climates, respectively. The bottom plots of Figure 1 are clear-sky Aqua MODIS images for each site. It is important to realize that the issue of representativeness in coastal locations, i.e., NSA and TWPC3, will offer further difficulty in constraining our clear-sky calculated fluxes. Due to the inherent inhomogeneity of coastlines, we do not expect the ARM-observed surface characteristics to necessarily represent the large CERES field of view (FOV), especially at the NSA site when sea ice and snow can exist within the FOV, while the snow has completely melted at the point location of the ground-based instrument. As demonstrated in the work of Dong *et al.* [2016] for Arctic stratus clouds, in order to

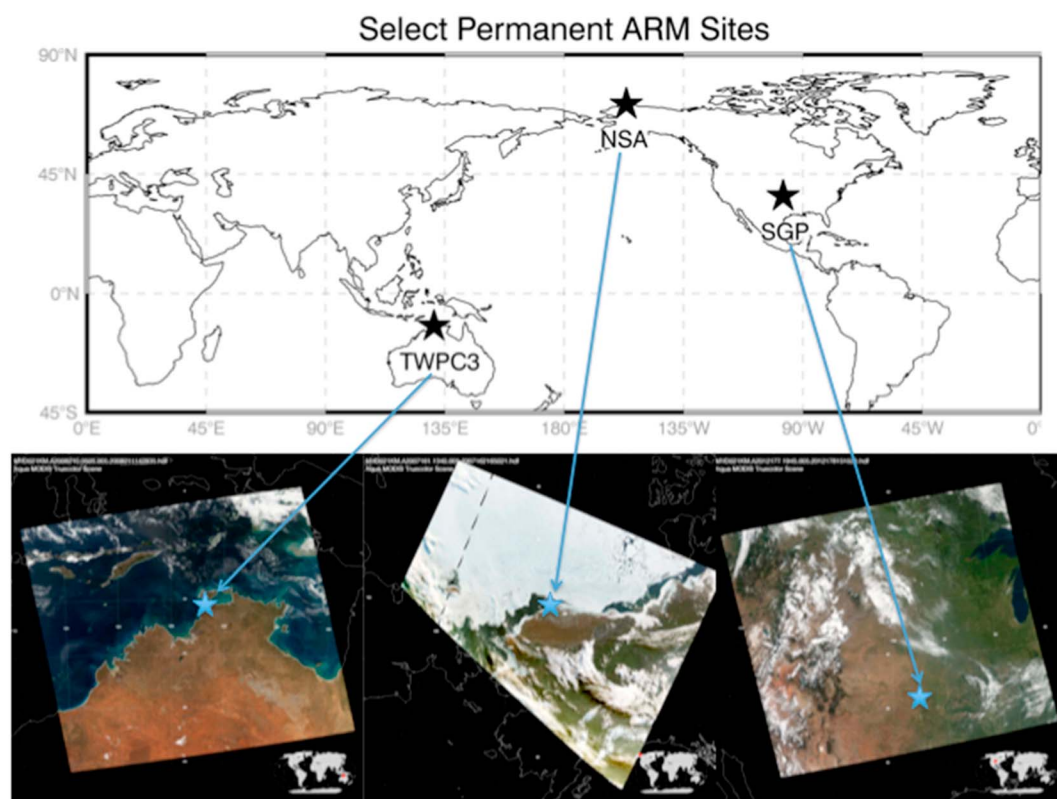


Figure 1. (top) The stars represent the locations of the three ARM sites selected for this study. The ARM Southern Great Plains (SGP; 36°36′18.0″N, 97°29′6.0″W); the North Slope Alaska (NSA; 71°19′23.73″N, 156°36′56.70″W); and Tropical Western Pacific (TWP) Darwin, Australia (C3; 12°25′28.56″S, 130°53′29.75″E) sites. (bottom) The Aqua MODIS images show examples of clear-sky cases at each site. The blue stars are the approximate locations of each site on the MODIS image granule.

achieve radiative closure at the surface and TOA over a $30 \times 30 \text{ km}^2$ domain, the ARM Eppley precision spectral pyranometer (PSP)-measured surface albedos at NSA must be adjusted (63.6% and 80% of the ARM surface albedos for snow-free and snow cases, respectively) to account for the land/sea contrast within the domain.

In this study, clear skies are verified by inspecting the Active Remote Sensing of Clouds (ARSCL) value-added product (VAP) [Clothiaux *et al.*, 2000]. This VAP is derived from a combination of Millimeter Cloud Radars (MMCRs), micropulse lidar, and laser ceilometer. MMCRs are vertically pointing radars operating at 8.6 mm and provide a continuous time series of cloud hydrometeors passing through the radar FOV, making it relatively easy to identify clear and cloudy scenes [Moran *et al.*, 1998]. Furthermore, the MMCRs can detect all types of clouds up to 16 km with a radar reflectivity ranging from -50 to $+20$ dBZ. Since a combination of lidar and ceilometer measurements can offer the best estimate of cloud base height, they are included in the algorithm [Clothiaux *et al.*, 2000].

Located at the three ARM sites are upward and downward looking standard Eppley precision spectral pyranometers (PSPs) and precision infrared pyrgeometers, which provide measurements of the surface downward (and upward) SW ($0.3\text{--}3 \mu\text{m}$) and LW ($4\text{--}50 \mu\text{m}$) radiative fluxes, as well as albedo, at 1 min intervals [Long and Shi, 2008]. Uncertainty estimates in the downward SW and LW radiative fluxes are 10 and 4 W/m^2 , respectively [Long and Shi, 2008]. These observed surface downward SW and LW fluxes are used to constrain the calculated fluxes in section 3.2. Measurements of surface skin temperature at the ARM SGP and NSA sites are also used for this study; skin temperature is not available at the ARM TWPC3 for the study time period. Therefore, we used the lowest level in the merged sounding as an approximation. The equivalent blackbody temperature is measured by a downward looking infrared thermometer ($9.6 \mu\text{m}$ to $11.5 \mu\text{m}$) and is accurate to within $\pm 0.5 \text{ K}$ [Morris, 2006].

High-resolution vertical profiles of temperature and water vapor are available from the ARM-merged sounding VAP. In its final form, the merged soundings are a combination of observations from radiosondes, microwave radiometers, surface-based meteorological instruments, and the European Centre for Medium-Range Weather Forecasts model output [Trojan, 2012]. Using a sophisticated scaling/interpolation/smoothing algorithm, thermodynamic variables are available at 1 min intervals with a total of 266 levels from the surface to ~50 hPa.

2.2. Satellite

2.2.1. Microwave Limb Sounder

Launched in 2004, the Aura satellite became the second member of the A-Train [L'Ecuyer and Jiang, 2010] array of satellites that observes the Earth in a Sun-synchronous, polar orbit ~15 times a day. Aura is equipped with the Microwave Limb Sounder (MLS) instrument [Waters *et al.*, 2006], which is designed to make high-quality measurements of upper atmospheric temperature, water vapor, ozone, and an assortment of other climate sensitive atmospheric constituents. The acceptable range of the retrieved temperature is 261–0.001 hPa with an estimated uncertainty of ~1 K when compared to other observations [Schwartz *et al.*, 2008]. The retrieved MLS temperature used for this study is from version 4.2, level 2 [Livesey *et al.*, 2015]. Stratospheric ozone from MLS is retrieved at a frequency of 240 GHz, which offers the best precision for a wide vertical range [Froidevaux *et al.*, 2008]. Intercomparison studies suggest that the ozone values from MLS match fairly well with multiinstrument means and Stratospheric Aerosol and Gas Experiment II values [Tegtmeier *et al.*, 2013]. The recommended range of the MLS ozone product is from 261 to 0.02 hPa with an estimated uncertainty of ~5–10%. The MLS ozone product used for this study is also from version 4.2, level 2. MLS water vapor is retrieved at a frequency of 190 GHz with acceptable range of 316–0.002 hPa. The estimated uncertainty of MLS water vapor in the stratosphere is ~10% [Read *et al.*, 2007]. In the upper troposphere the estimated MLS water vapor uncertainty is 20% in the tropics and midlatitudes and ~50% at high latitudes (>60°N/S) [Read *et al.*, 2007; Jiang *et al.*, 2012]. The MLS version 4.2, level 2 water vapor product is used for this study.

2.2.2. Atmospheric Infrared Sounder (AIRS)

AIRS is aboard on the Aqua satellite, which was launched in 2002 for the advancement and support of knowledge related to climate research and weather forecasting. The AIRS sensor is a cross-track scanning hyperspectral (2378 bands) spectrometer covering infrared wavelengths (3.7–15.4 μm). For this study, the level 3, version 6 daily $1^\circ \times 1^\circ$ gridded product is used for tropospheric ozone estimates at standard pressure levels [Tian *et al.*, 2014]. Biases in the AIRS-retrieved ozone are estimated to be less than 5% when compared to collocated ozonesonde profiles and World Ozone and Ultraviolet Radiation Data Center data sets [Divakarla *et al.*, 2008].

2.2.3. CERES Aqua Single Scan Footprint Edition 4A

Satellite TOA radiative fluxes are estimated from the CERES Aqua Single Scan Footprint (SSF) edition 4 product since 2002 [Geier *et al.*, 2001; Loeb *et al.*, 2003]. Satellite-measured radiances are from a SW channel (0.3–5 μm), a window channel (8–12 μm), and a total channel (0.3–100 μm) [Wielicki *et al.*, 1996]. TOA SW radiances are then converted to fluxes using angular distribution models [Su *et al.*, 2015a], which take into account solar zenith angle, viewing zenith angle, and relative azimuth angle. The MODIS imager supplements CERES to provide more details regarding clouds and aerosols. The collocation of clouds, aerosols, and radiation information is a major benefit to the SSF product. Included in the SSF product are estimates of clear-sky fraction, which is used for cloud screening purposes, as described in section 2.3. TOA SW and LW flux root-mean-square errors are estimated to be less than 6% for a variety of scene types [Loeb *et al.*, 2006; Su *et al.*, 2015b]. Instantaneous footprints of TOA radiances are used as a constraint to the calculated fluxes presented in section 3.2.

2.3. Generated Hybrid Atmospheric Profiles From ARM and Satellite Observations

Profiles of atmospheric temperature, water vapor mixing ratio, and ozone mixing ratio have been generated from ARM-merged sounding and satellite (MLS and AIRS) retrievals over three ARM sites, which are used to evaluate the MERRA-2 profiles. These generated profiles will henceforth be referred to as the hybrid profiles. The hybrid profiles are also used as input to the radiative transfer model to calculate clear-sky surface and TOA radiative fluxes for the radiation closure study. A-Train satellite overpasses within a $120 \times 120 \text{ km}^2$ box centered at each ARM site are first determined for the period of August 2004 to December 2013. Once the overpass days are found, a two-step cloud screening process can be performed.

Table 1. The Number of Clear-Sky Cases Selected for This Study at Each Site During the August 2004 to December 2013 Period

	SGP	NSA		TWPC3
		Snow ($\alpha \geq 0.3$)	Snow-Free ($\alpha < 0.3$)	
Total no. of cases	51	12	5	13
No. of daytime	19	7	5	9
No. of nighttime	32	5	0	4

First, the ARM ARSCL cloud product is used to screen for clouds within a 3 h period centered on the satellite overpass time. A clear-sky case is identified using a combination of the ARM ground-based MMCR, ceilometer, and lidar observations during the 3 h period. Once clear-sky cases are identified by the ARM ground-based

observations, a secondary clear-sky screening is performed through the inspection of the CERES SSF-derived, clear-sky fraction. If the CERES-derived clear-sky fraction in the $120 \times 120 \text{ km}^2$ area centered on the ARM site is greater than $\sim 95\%$, these clear-sky cases can be used in this study. After the clear-sky cases are identified and selected, the vertical profiles of temperature, ozone mixing ratio, and water vapor mixing ratio are generated for each clear-sky case. Tropospheric profiles of temperature and water vapor are from the ARM-merged soundings (surface to 100 hPa), while ozone is from AIRS (surface to 260 hPa). All upper atmospheric profiles are from MLS.

Table 1 lists the number of cases identified for this study at each ARM site from August 2004 to December 2013, where a total of 51 cases are selected at the ARM SGP site and 13 cases at the ARM TWPC3 site. Polar-orbiting satellites, such as those in the A-Train, scan the high latitudes with relatively high frequency. However, the cloud frequency of occurrence at the ARM NSA is rather large (76% [Dong *et al.*, 2010]), limiting the total number of available clear-sky cases to 17.

2.4. Modern-Era Retrospective Analysis for Research and Applications, version 2 (MERRA-2)

A new version of MERRA has been released with several major improvements, making it the centerpiece of the evaluation performed in this study. The Goddard Earth Observing System version 5.12.4 (GEOS 5) now uses a three-dimensional variational algorithm during the data assimilation process. MERRA-2 is horizontally discretized on a cubed sphere grid, which is superior to the latitude-longitude methods used in earlier versions [Bosilovich *et al.*, 2015]. For MERRA-2 the number of assimilated observations per 6 h increment has increased from three million in 2010 to five million in 2015; however, capabilities of assimilating future satellite observations are also developed. This is in contrast to the one and a half million observations assimilated in MERRA from 2002 to the present. MERRA-2 is available on a $0.5^\circ \times 0.625^\circ$ grid with 72 hybrid-eta levels from the surface to 0.01 hPa as instantaneous and time-averaged products at synoptic (0, 6, 12, and 18 UTC) and midsynoptic times (3, 9, 15, and 21 UTC).

One of the major improvements in MERRA-2 includes the minimization of abrupt variations in global interannual states (e.g., temperature) due to changes in observing system. This is accomplished by constraining the global dry mass balance, which permits the global changes in water by the analysis increment to be near zero [Takacs *et al.*, 2016]. Also, land-surface hydrology is improved by forcing precipitation through an observation-corrected field rather than a model-corrected field [Reichle and Liu, 2014]. In terms of the zonal temperature, MERRA-2 is within 1 K of its previous version. In the middle to upper troposphere, differences of up to 0.6 K are seen in the tropics with MERRA-2 being slightly warmer [Bosilovich *et al.*, 2015]. Differences in the tropical tropospheric temperature are consistent with the additional radiative heating related to excess tropical cloud cover. An increase in tropospheric humidity is achieved in MERRA-2, likely a result of increased reevaporation rates of frozen precipitation [Molod *et al.*, 2015].

The 3 h instantaneous vertical profiles of temperature, water vapor mixing ratio, and ozone mixing ratio (inst3_3d_asm_Np; doi:10.5067/QBZ6MG944HW0) from the closest grid point (in time and space) are used for the evaluation and RTM calculations. Differences in the vertical profiles are expected since the MERRA-2 profiles cannot be perfectly collocated with the satellite/ground-based data.

2.5. NASA Langley Research Center-Modified Fu-Liou Radiative Transfer Model (RTM) for CERES Edition 4 Products

Calculating clear-sky (no clouds but including aerosols) surface and TOA radiative fluxes is accomplished by running the NASA Langley-modified Fu-Liou RTM [Fu and Liou, 1993; Kato *et al.*, 2005]. Access to the source

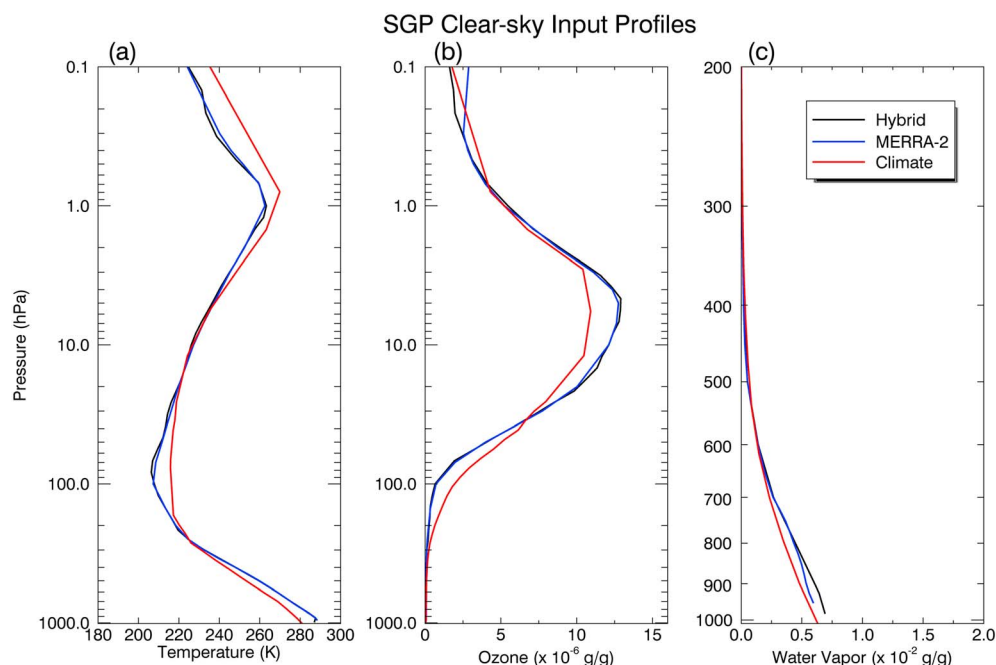


Figure 2. Vertical profiles of (a) temperature, (b) ozone mixing ratio, and (c) water vapor mixing ratio at the ARM SGP site. These profiles represent the clear-sky cases only during the August 2004 to December 2013 period (from Table 1). The black line represents the hybrid profiles from the ARM-merged soundings (below 100 hPa) and the Microwave Limb Sounder (MLS) for atmospheric temperature and water vapor. The ozone profile (below 260 hPa) is from the Atmospheric Infrared Sounder (AIRS) and MLS. The blue line is from the closest MERRA-2 grid point, and the red line is the midlatitude climatological mean.

code can be found at <http://www-cave.larc.nasa.gov/cgi-bin/lfcode/accessfl.cgi>. Infrared and solar radiative fluxes are calculated with several options: a δ -four- or δ -two/four-stream solver and a δ -two, δ -four, or gamma-weighted δ -two-stream solver, respectively [Kato *et al.*, 2005]. This study utilizes the two-stream solver for SW calculations, while the two/four-stream solver is used for the LW. For the SW and LW fluxes a total of 18 and 14 bands are computed, respectively, and are sensitive to specific gaseous species. A total of 25 different aerosol types are featured in this model and are characterized by their own spectral normalized extinction, scattering, and absorption properties.

To calculate the clear-sky SW and LW fluxes at the surface and TOA, the RTM requires inputs of temperature, ozone mixing ratio, and water vapor mixing ratio profiles from the surface to 0.1 hPa. Other information, such as solar zenith angle, surface albedo, skin temperature, and aerosol optical depth (AOD) at a certain wavelength for each selected case, are also required. For this study, the cloud information is filtered out, and the characteristic surface LW emissivity is changed to 0.975.

3. Results and Discussions

The hybrid profiles are used to evaluate the suitability of using MERRA-2 vertical profiles of temperature, ozone mixing ratio, and water vapor mixing ratio for computing surface, TOA, and in-atmosphere radiative fluxes with the Fu-Liou RTM. We also compare how the RTM-calculated fluxes differ based upon the hybrid, MERRA-2, or climatological mean profiles, assuming that surface characteristics are held constant. The climatological mean profiles are from the World Meteorological Organization and are made available with the RTM source code. While these profiles are for all-sky conditions, they offer an additional measure for assessing the sensitivity of RTM-calculated fluxes to atmospheric profiles.

3.1. Evaluation of MERRA-2 Clear-Sky Atmospheric Vertical Profiles

Figure 2 presents the clear-sky vertical profiles of temperature, ozone mixing ratio, and water vapor mixing ratio for the 51 selected cases at the ARM SGP site. Despite the inherent unrepresentativeness between

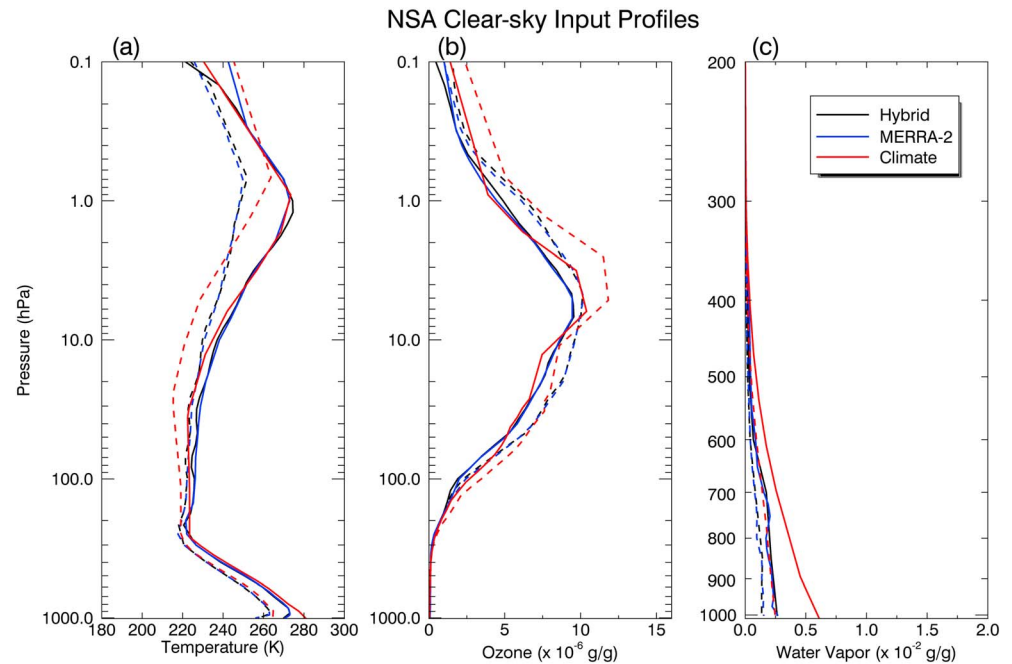


Figure 3. Same as Figure 2 but for the vertical profiles at the ARM NSA site. The solid lines are for snow-free cases (surface albedo <0.3), whereas the dashed lines are for snow cases (surface albedo ≥ 0.3). The red line represents the Arctic climatological mean.

the MERRA-2 grid box ($0.5^\circ \times 0.625^\circ$) and the point of the hybrid profile, the temperature profiles match very well (within 2%) through the atmospheric column and their differences are nearly indistinguishable (Figure 2a). The midlatitude climatological mean temperature, however, is slightly colder than the hybrid and MERRA-2 temperatures below ~ 300 hPa and is too warm from ~ 200 to 15 hPa and above 4 hPa. Since stratospheric ozone is directly assimilated into MERRA-2, it is not surprising that the hybrid and MERRA-2 ozone profiles in Figure 2b match very well. On the other hand, MERRA-2 does not assimilate tropospheric ozone, which allows for differences of up to 200–400% for some cases (not shown). The midlatitude climate mean ozone mixing ratio is less than the hybrid and MERRA-2 profiles in the middle to upper stratosphere but is slightly larger in the upper troposphere and lower stratosphere.

Lastly, the clear-sky water vapor mixing ratios at the ARM SGP site are shown in Figure 2c. Since the water vapor mixing ratios are relatively small above the troposphere, the profiles are presented at ~ 1000 –200 hPa for enhanced clarity. The hybrid and MERRA-2 water vapor mixing ratios match very well above ~ 850 hPa. However, below 850 hPa, the MERRA-2 water vapor profile diverges from the hybrid profile to the drier side by $<0.25 \times 10^{-2}$ g/g. On the global scale, a moist bias in MERRA-2 can be up to 75–150% in the upper troposphere [Jiang et al., 2015] when compared to AIRS and MLS. The midlatitude climate mean water vapor mixing ratio is less than both the hybrid and MERRA-2 profiles in the lower troposphere (below 700 hPa).

Similar to Figure 2, the vertical profiles of temperature, ozone, and water vapor mixing ratio for the ARM NSA site are illustrated in Figure 3. Note that the solid lines represent the average profile from the 5 selected snow-free cases and the dashed lines are for the 12 snow cases at this site. The distinction between the snow and snow-free cases is made because of their contrasting atmospheric and surface conditions. The primary source of moisture for this region is restricted when sea ice and snow cover persist in the Arctic Ocean. This will affect not only cloud formation (although not a process we are concerned with in this paper) but also heat and atmospheric energy transport [Hwang et al., 2011].

The MERRA-2 temperature profiles (Figure 3a) for both the snow and snow-free cases at the ARM NSA site show an excellent agreement with the hybrid profiles through most of the troposphere and stratosphere. For the snow-free cases, the MERRA-2 temperature is slightly colder just below the stratopause (~ 1 –2 hPa) and warmer above 0.3 hPa by ~ 20 K. Nevertheless, MERRA-2 is able to reproduce the low-level temperature

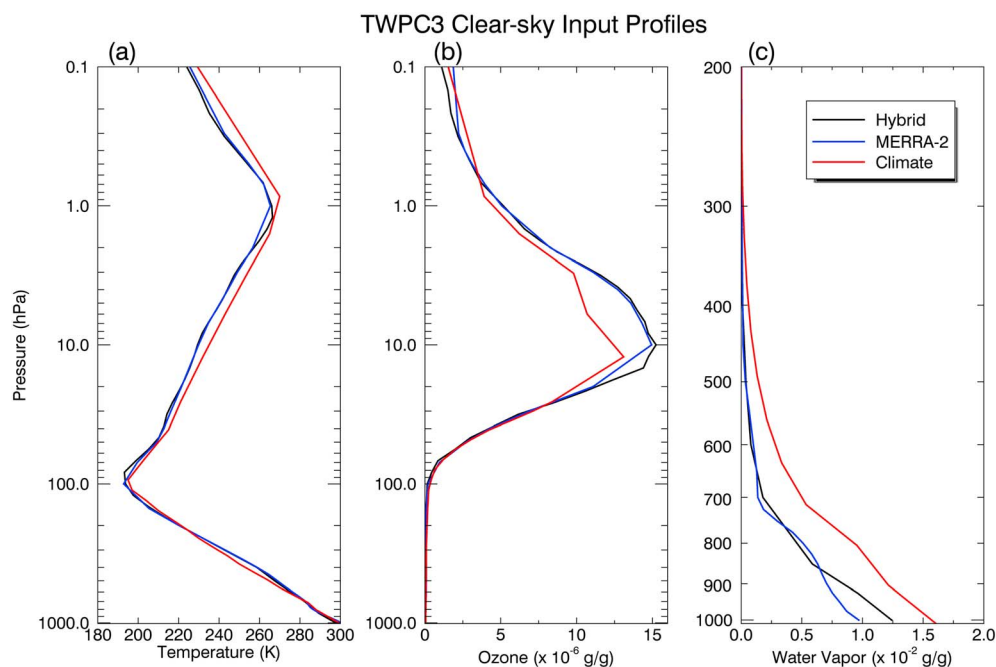


Figure 4. Same as Figure 2 but for the vertical profiles at the ARM TWPC3 site. The red line represents the tropical climatological mean.

inversion for both snow and snow-free cases. The Arctic climate mean temperature is warmer in the troposphere and colder in the stratosphere for the snow-free cases and does not suggest a low-level inversion. A typical decrease in temperature is observed through the shallow troposphere at the NSA site for a snow-covered surface, whereas in the stratosphere, a rather isothermal temperature structure is seen in both the hybrid and MERRA-2 profiles. The temperature change through the stratosphere is only ~ 20 K when the surface albedo is greater than 0.3, as opposed to the $60+$ K change in the snow-free cases. Climatologically, the temperature matches well with the hybrid profile in the troposphere for snow cases but diverges greatly in the upper atmosphere.

Ozone in the Arctic is depleted more efficiently during the northern hemisphere summer months. Therefore, the stratospheric ozone mixing ratios for the snow cases are larger than those of the snow-free cases as shown in Figure 3b. Similar to the ozone comparison at the SGP site, the MERRA-2 and hybrid profiles match very well through the whole column.

As previously stated, water vapor in the Arctic has a strong seasonal dependence due to the variation of sea ice coverage. As expected, the water vapor mixing ratios from the snow-free cases are larger than those from the snow cases. For the snow cases, the water vapor mixing ratios are almost constant ($\sim 0.15 \times 10^{-2}$ g/g) through the entire troposphere, which is well replicated in MERRA-2. Once the sea ice has begun to retreat (i.e., the snow-free cases), the atmospheric water vapor mixing ratios increase in all three profiles. The climate mean water vapor mixing ratio is much too moist and almost twice as large as the hybrid and MERRA-2 values through the troposphere. However, this result is expected as the climatological mean profiles are for all-sky conditions.

Finally, Figure 4 illustrates the temperature, ozone, and water vapor mixing ratio profiles at the TWPC3 ARM site. Darwin is located directly on the northern coast of Australia; therefore, coastal processes (e.g., land/sea breezes) modify the atmospheric conditions at this site. Temperature (Figure 4a) is well reproduced in MERRA-2 at the TWPC3 site through the troposphere; however, a slight discrepancy is seen just above the tropopause and below the stratopause, which could be an artifact of the coarser vertical resolution of MERRA-2. The tropical climate mean temperature agrees well with the hybrid and MERRA-2 profiles in the troposphere but is slightly warmer in the stratosphere and mesosphere. The TWPC3 ozone comparison is similar to the results at the ARM SGP and NSA sites, where the ozone profiles from MERRA-2 and the hybrid data set

Table 2. Averaged Surface Albedos and AODs From the Selected Cases at the Three ARM Sites^a

	SGP	NSA		TWPC3
		Snow ($\alpha \geq 0.3$)	Snow-Free ($\alpha < 0.3$)	
Surface α	0.209	0.796	0.225	0.163
AOD	0.122	0.076	0.067	0.137

^aFor cases without an AOD observation, the AERONET 500 nm mean value was used (0.14, 0.08, and 0.14 for SGP, NSA, and TWPC3, respectively).

are very close. Yet still, a noticeable discrepancy between the two data sets can be seen from ~10 to 20 hPa, where MERRA-2 is slightly smaller.

Tropospheric water vapor at the ARM TWPC3 site is modified by the adjacent oceanic environment through transport by mesoscale features (e.g., land/sea breezes) and general circulation patterns. For the 13 selected cases at this site, all

three water vapor mixing ratios are much higher than those at the ARM SGP and NSA sites. Both the hybrid and MERRA-2 water vapor mixing ratios are much drier than the tropical climatological mean through the troposphere by $<0.6 \times 10^{-2}$ g/g, again likely due, in part, to the fact that the climate mean profile is for all skies. It is expected that the unrepresentativeness between the MERRA-2 grid box and the ARM point location may lead to their relatively large difference (1000–3500% for several cases; not shown), especially since the TWPC3 site is located directly on the coast.

Through the comparisons made in three different climatic regimes, we can make the following conclusions. The MERRA-2 atmospheric temperature profiles are nearly identical to the hybrid ones, and the climate mean temperature profiles agree with the hybrid ones within several kelvin. Since MLS ozone data are directly assimilated into MERRA-2, it is not surprising that the MERRA-2 and hybrid ozone profiles match extremely well at all three ARM sites. Most of the MERRA-2 water vapor mixing ratios agree well with the hybrid ones over three sites except for in the boundary layer at the ARM TWPC3.

3.2. A Radiation Closure Study

The clear-sky surface and TOA radiative fluxes are calculated using the NASA Langley-modified RTM with inputs from three different profile data sets at three ARM sites. For the clear-sky cases selected in this study, only the vertical profiles of temperature, ozone mixing ratio, and water vapor mixing ratio are required as input, along with the solar zenith angle, surface albedo, AOD (including aerosol type), skin temperature, and a Sun-Earth distance correction coefficient. In this study, the surface and TOA radiative fluxes are calculated for each clear-sky case at each site with the same surface characteristics but with different vertical profiles of temperature, ozone, and water vapor from the hybrid, MERRA-2, and climate mean.

Table 2 lists the average ARM-measured surface albedos and Aerosol Robotic Network (AERONET) AODs for the identified clear-sky cases at three ARM sites selected for this study. At the ARM SGP and NSA sites, we assume a continental aerosol, while at the TWPC3 site an urban aerosol is assumed in the RTM calculations (consider these aerosols as type 1). The average ARM-observed surface albedos are 0.209, 0.225 (0.796), and 0.163 at the SGP, NSA for snow-free (snow), and TWPC3 sites, respectively. The AOD (500 nm) values are 0.122, 0.076 (0.067), and 0.137, respectively. Case-specific AOD's come from AERONET observations when they are available; otherwise the climatological mean is used. Both the surface albedo and AOD have a significant impact on both the TOA-reflected SW flux (SW_{up}) and downward SW flux (SW_{dn}) at the surface. The predominant aerosol types observed at these three locations include nitrates, sulfates, sea salt, smoke, and dust [Quinn *et al.*, 2002; Alexandrov *et al.*, 2005; Qin and Mitchell, 2009].

Table 3 lists the means of the observed and RTM-calculated SW and LW fluxes at the TOA and surface with inputs from the atmospheric profiles over three ARM sites. The untuned calculated fluxes show that the smallest differences (~ 10 W/m²) to observations occur at the ARM SGP, and the largest differences (> 50 W/m²) happen at the ARM TWPC3. This is not so surprising, as the land surface around the ARM SGP is fairly homogeneous in comparison to the other two sites; the ARM PSP-measured surface albedos are relatively close to the mean albedo over the 120×120 km² domain. In contrast, the ARM TWPC3 and NSA sites are located directly on the coast. The ARM PSP-measured surface albedos at these two sites cannot effectively represent the domain average albedos as discussed by Dong *et al.* [2016]. Therefore, we must adjust the ARM surface

Table 3. The Averaged Surface and TOA Radiative Fluxes (W/m^2) From ARM/CERES Observations and Untuned/Tuned RTM Calculations With Inputs From the Three Profile Types

	TOA SW_up		TOA LW_up		Surface SW_dn		Surface LW_dn	
	Untuned	Tuned	Untuned	Tuned	Untuned	Tuned	Untuned	Tuned
SGP								
Hybrid	176.67	166.31	273.54	273.49	682.68	674.66	299.76	299.86
MERRA-2	177.37	166.84	273.05	273.00	689.97	681.95	292.86	292.96
Climate	173.49	163.43	259.59	259.54	667.88	660.09	275.17	275.26
Observations	165.31		273.16		672.44		302.55	
NSA snow ($\alpha \geq 0.3$)								
Hybrid	170.96	143.46	194.12	194.03	168.55	164.80	155.88	156.53
MERRA-2	170.98	143.44	193.20	193.11	168.73	164.93	155.00	155.67
Climate	162.90	136.92	190.42	190.39	160.48	157.01	183.73	184.34
Observations	145.67		195.61		160.48		159.58	
NSA snow-free ($\alpha < 0.3$)								
Hybrid	103.30	116.30	251.59	251.26	351.49	351.26	248.78	249.27
MERRA-2	103.47	116.53	246.85	246.70	352.53	352.27	245.71	246.22
Climate	100.02	112.40	247.92	247.80	337.83	337.69	299.36	299.75
Observations	118.93		247.02		352.38		248.24	
TWPC3								
Hybrid	168.06	121.30	311.37	308.26	789.10	769.13	355.38	358.95
MERRA-2	169.77	122.20	311.75	308.59	797.82	777.70	353.68	358.04
Climate	164.13	118.93	286.67	284.41	765.65	746.44	398.21	400.34
Observations	116.83		312.99		758.04		376.35	

albedos to account for the land/sea contrast within the domain in order to reach radiative closure at both the surface and TOA (Appendix A).

Dong et al. [2016] provided a method to calculate the domain average albedo based on the ARM NSA PSP-measured surface albedos and adjacent ocean albedo (~ 0.06), as well as the percentages of water and land. For snow-free cases, they found that the domain mean albedo is 63.6% of the ARM measurements, which was used in their study to reach radiative closure for both the surface and TOA radiation budgets. For snow cases, they discussed three possible conditions, such as an open ocean, an ocean with sea ice containing open leads, and an ocean that is completely covered by sea ice or snow, with albedos similar to the ARM PSP measurements (~ 0.8). The domain mean albedos are different for these three conditions; however, the ARM PSP-measured surface albedos for snow cases were adjusted by 80% in the work of *Dong et al.* [2016]. In this study, we follow a similar method as *Dong et al.* [2016] to tune the ARM PSP-measured surface albedos to account for the water and land components of the domain; this is done to reach radiative closure at the surface and TOA over the ARM NSA and TWPC3 sites.

Table 4 offers the adjustments used to match the RTM-calculated radiative fluxes to within $\sim 5 \text{ W/m}^2$ of the observations when using the hybrid profiles as input. Admittedly, some of these values have been arbitrarily chosen in order to achieve the closest match between the calculated and observed fluxes (namely, $\text{AOD}_2/\text{AOD}_1$). To be clear, the aerosol ratio ($\text{AOD}_2/\text{AOD}_1$) is the ratio of the AOD for aerosol type 2 to that of the aerosol type 1. The aerosol type 2 at the ARM SGP is urban, while at the NSA and TWPC3 sites it is maritime. With the inclusion of a secondary aerosol type, we are able to adjust the surface and TOA fluxes almost independently.

At the SGP site, the ARM PSP-measured surface albedo is reduced by 10%, which will account for some of the surface inhomogeneity in the CERES FOV centered at the ARM site. A majority of the surface inhomogeneity is attributed to crop type (e.g., wheat, grass, soybean, and alfalfa [*Li et al.*, 2002]). The aerosol ratio is set to 40% at the ARM SGP site.

The surface albedo is also reduced (by 20%) at the ARM NSA site for the snow cases, following the conclusion in *Dong et al.* [2016], which may account for the different albedos from old and fresh snow surfaces and the nearby open water and leads [*Brandt et al.*, 2005]. An increase in albedo of 20% is applied for the snow-free cases at the NSA site, which is contrary to the conclusion in *Dong et al.* [2016]. This change accounts for the

Table 4. Applied Changes (%) to the Observed Surface Albedo and AOD for the Two Types of Aerosols Used to Tune the RTM-Calculated Fluxes to Match the Observations

	SGP	NSA		TWPC3
		Snow ($\alpha \geq 0.3$)	Snow-Free ($\alpha < 0.3$)	
$\Delta SFC \alpha$ (%)	−10	−20	+20	−50
AOD_2/AOD_1	0.40	0.20	0.20	0.99

sea ice observed by the large satellite FOV, while the ARM PSP-measured surface albedos are below 0.3. Although the maximum albedo threshold for snow-free cases is 0.3, this number represents the ARM site only. Again, the CERES FOV over the ARM NSA site is much larger than the point observation and may include snow surfaces and sea ice within a grid box of $120 \times 120 \text{ km}^2$, which will increase the albedo of the footprint. By visually investigating MODIS images for the five selected snow-free cases, we can confirm that sea ice and snow surfaces are partially present within the $120 \times 120 \text{ km}^2$ domain centered on the NSA ARM site. The aerosol ratio is set to 20% for both snow-free and snow cases in this study.

In order to match the calculated SW fluxes to the observed values at TWPC3, the albedo is reduced (by 50%) to account for the relatively small ocean surface albedo within the domain. Since the ARM TWPC3 site is located directly on the coast, there exists a strong albedo contrast between the land surface (~ 0.16) and ocean (0.06), similar to the NSA snow-free cases, but the actual percentage is dependent on the land and water coverage within the domain. At the TWPC3 site, the aerosol ratio is set to 99%.

While adjusting the surface albedo and AODs described above, better agreements between the mean calculated fluxes and the observed values at each site are achieved and illustrated in Figure 5b (compared to the untuned results in Figure 5a). Note that each point in Figure 5 depicts the average flux difference (RTM calculated minus observed) from all cases at each site using inputs from the hybrid, MERRA-2, and climate mean profiles. Many of the symbols fall outside of the dashed lines (a bias of greater than 5 W/m^2) in Figure 5a; however, some of these larger biases disappear in Figure 5b. After tuning (Figure 5b), most of the calculated radiative fluxes using the hybrid and MERRA-2 input profiles are within 5 W/m^2 of the observations.

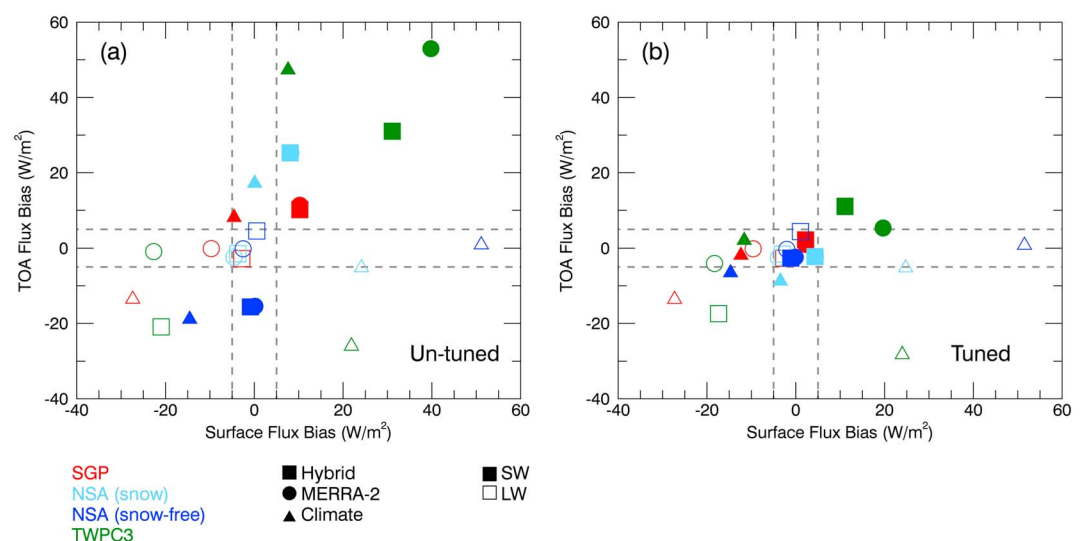


Figure 5. The flux differences (calculation minus observation) between the ARM/CERES observations and Fu-Liou radiative transfer model (RTM) calculated fluxes with input from the hybrid (black square), MERRA-2 (black circle), and climate mean profiles (black triangle) at the surface (x axis) and top of atmosphere (TOA) (y axis). The symbols are color coded for each site (red: SGP, light blue: NSA snow case, blue: NSA snow-free cases, and green: TWPC3). (a) The untuned result and (b) the result after tuning for the calculated shortwave (filled symbols) and longwave (open symbols) fluxes.

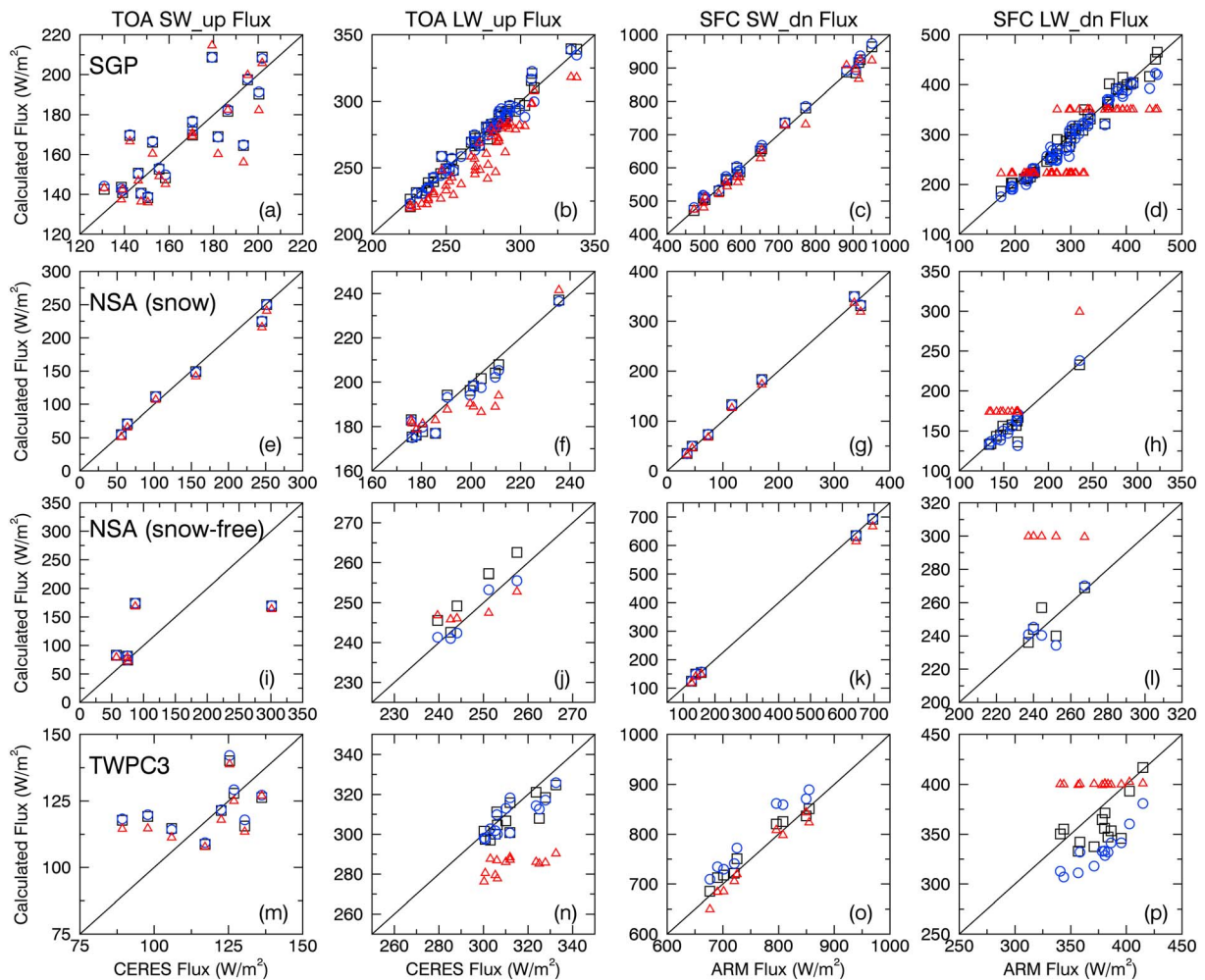


Figure 6. Scatterplots of the ARM/CERES-observed fluxes versus the tuned RTM-calculated fluxes from the three input profiles (black: hybrid; blue: MERRA-2; red: climate mean). Each symbol corresponds to a specific clear-sky case. Results are shown for all three sites (a–d) SGP, (e–h) NSA-snow cases, (i–l) NSA-snow-free cases, and (m–p) TWPC3. From left to right, the columns represent the TOA SW_{up}, TOA LW_{up}, surface SW_{dn}, and surface LW_{dn} flux comparisons.

For enhanced clarity to the results in Figure 5, Table 3 lists the averaged surface and TOA radiative fluxes from the ARM/CERES observations and untuned/tuned RTM calculations with input from the three profiles at the three ARM sites. For example, the untuned calculated surface and TOA SW and LW fluxes at the SGP site using the hybrid profiles (red filled and open squares in Figure 5a) agree with the observed fluxes to within 11 W/m^2 ; however, the differences become less than 3 W/m^2 after tuning. In general, our tuning parameters (surface albedo and AOD) can reduce the biases in the calculated SW fluxes but not for LW fluxes. The LW fluxes are mainly determined by atmospheric temperature and water vapor profiles and skin temperature, not by surface albedo and AOD. For example, at SGP, the large negative bias in the climate mean-calculated surface LW_{dn} flux can be attributed to its relatively cold tropospheric temperatures and relatively dry tropospheric water vapor mixing ratio as shown in Figure 2. Nevertheless, the average error in the tuned surface LW_{dn} flux from the hybrid profiles is less than 3 W/m^2 , which is consistent with Long and Turner [2008]. However, the TOA LW_{up} flux is also negatively biased despite the warmer stratosphere/mesosphere in the climate mean profile. Therefore, we can say with confidence that other parameters (e.g., skin temperature) affect the TOA LW_{up} flux, and an additional study is warranted to determine the sensitivity. For the 12 selected snow (surface albedo ≥ 0.3) cases at the ARM NSA site, the positive bias in surface LW_{dn} flux using climate mean profiles can be up to $\sim 25 \text{ W/m}^2$. This result is likely due to the relatively large tropospheric water vapor and warmer temperature in the climatological Arctic

Table 5. The 90% Confidence Intervals for the Average Tuned RTM-Calculated Fluxes (W/m^2) [μ_{lower}^* , μ_{upper}^*]^a

	TOA SW _{up}		TOA LW _{up}		Surface SW _{dn}		Surface LW _{dn}	
	Interval	%	Interval	%	Interval	%	Interval	%
SGP								
Hybrid	[157.20, 175.42]	10.96	[266.98, 280.00]	4.76	[608.19, 714.13]	19.70	[282.30, 317.42]	5.21
MERRA-2	[157.77, 175.91]	10.87	[266.57, 279.43]	4.71	[615.21, 748.69]	19.57	[276.43, 309.49]	4.85
Climate	[153.85, 173.01]	11.72	[253.27, 265.81]	4.83	[594.02, 726.16]	20.02	[260.31, 290.21]	4.53
NSA snow ($\alpha \geq 0.3$)								
Hybrid	[84.54, 202.38]	82.14	[184.69, 203.37]	9.62	[69.18, 260.42]	133.30	[142.78, 170.28]	16.69
MERRA-2	[84.47, 202.41]	82.22	[184.09, 202.13]	9.34	[69.00, 260.86]	133.75	[140.67, 170.67]	18.19
Climate	[79.67, 194.17]	83.63	[181.73, 199.05]	9.10	[64.17, 249.85]	135.61	[165.55, 203.13]	23.94
NSA snow-free ($\alpha < 0.3$)								
Hybrid	[67.96, 164.64]	83.13	[243.35, 259.17]	6.30	[78.16, 624.36]	155.50	[236.31, 262.23]	7.38
MERRA-2	[68.06, 165.00]	83.20	[239.96, 253.44]	5.46	[78.56, 625.98]	155.40	[232.88, 259.56]	7.57
Climate	[65.71, 159.09]	83.08	[245.07, 250.53]	2.20	[73.03, 602.35]	156.75	[299.59, 299.91]	0.10
TWPC3								
Hybrid	[115.60, 127.00]	9.40	[303.68, 312.84]	2.97	[726.11, 812.15]	11.19	[347.37, 370.53]	3.01
MERRA-2	[116.22, 128.18]	9.78	[304.12, 313.06]	2.90	[733.53, 821.87]	11.36	[348.02, 368.06]	2.58
Climate	[112.92, 124.94]	10.11	[282.23, 286.59]	1.54	[701.92, 790.96]	11.93	[399.94, 400.74]	0.11

^aThe percent is defined as $[(\mu_{\text{upper}}^* - \mu_{\text{lower}}^*)/\bar{X}] \times 100\%$. The bolded values contain $\geq 50\%$ of the individual cases.

winter profiles. The average calculated fluxes using the climate mean profile inputs continue to show some problems at the NSA site for the five snow-free cases. For instance, the calculated surface SW_{dn} and LW_{dn} fluxes are biased by approximately -15 and $+50 \text{ W/m}^2$, respectively. Greater absorption of both the SW and LW radiation is realized through the relatively large tropospheric water vapor mixing ratio, a result that could be attributed to the fact that the climate mean profile is for all skies. The large surface LW_{dn} bias could also be affected by the temperature profile, which is too large in the troposphere and does not resolve the low-level temperature inversion.

The green symbols in Figure 5 represent the averaged biases at the ARM TWPC3 site. A bias of greater than -20 W/m^2 is found in the surface LW_{dn} flux using the hybrid and MERRA-2 profiles, a result that is inconsistent with Long and Turner [2008] and is likely due to the skin temperature used in the RTM. In contrast to this large negative bias, the surface LW_{dn} flux calculated using the tropical climate mean profiles is positively biased by about the same amount. Because the tropospheric temperatures from three data sets at the ARM TWPC3 site are similar to each other, the large positive bias in the calculated surface LW_{dn} flux is most likely due to the moister climate mean tropospheric water vapor as shown in Figure 4c. This result is consistent with the findings in Dong *et al.* [2006], where the atmospheric water vapor plays an important role to the downward LW flux at the surface, but is insignificant to the downward SW flux at the surface. The opposing biases from the three input profiles suggest that the actual atmospheric water vapor should fall between them. The large negative bias ($\sim -26 \text{ W/m}^2$) in the TOA LW_{up} flux can also be attributed to the larger climate mean tropospheric water vapor, as the moister atmosphere absorbs more LW radiation emitted by the surface. Also, as previously stated, the skin temperature used in the calculation at TWPC3 is from the lowest level of the ARM-merged sounding because IR thermometer data are not available at TWPC3 during the study period. Assuming a typical lapse rate, the skin temperature would be larger than the ones used in this study. As such, if the actual skin temperatures were to be used, we expect a smaller absolute bias in the TOA LW_{up} flux at TWPC3. Moreover, Moy *et al.* [2010] have found that daytime variability in the calculated TOA LW_{up} flux can be reduced if satellite footprint estimates of skin temperature were used in lieu of point measurements. This finding may help to justify the large error in surface LW_{dn} flux in this study.

Figure 5 and Table 3 provide an overall summary of the comparisons between the average RTM-calculated and RTM-observed radiative fluxes, which may obscure some detailed information, such as large compensating errors from several cases. Therefore, we generate Figure 6 to detail the individual clear-sky cases for each parameter at each site. It is apparent that not all of the calculated fluxes are biased equally or in the same direction. For example, in Figure 6a the calculated clear-sky TOA SW_{up} fluxes at SGP are both positively and negatively biased against the CERES instantaneous fluxes by nearly 30 W/m^2 for some cases. However,

the average bias is only 1–2 W/m². A similar statement can be made about the calculated TOA SW_{up} fluxes at NSA (snow-free cases; Figure 6i) and TWPC3 (Figure 6m) and the surface LW_{dn} fluxes at SGP (Figure 6d) and TWPC3 (Figure 6p). On the other hand, the fluxes calculated with the climate mean profiles have a tendency of being biased either too high or too low (e.g., Figures 6b, 6h, 6l, and 6n).

Table 5 summarizes the 90% confidence intervals for the calculated surface and TOA, SW, and LW radiative fluxes. These values are calculated based upon the Student's *t* distribution as

$$-t < \frac{\bar{X} - \mu^*}{\sigma/\sqrt{n}} < t,$$

where \bar{X} is the mean-calculated flux, σ is the standard deviation of the calculated flux for all cases, n is the number of cases, and μ^* provides the upper and lower limits of the confidence interval (based on the value of $\pm t$). The relatively small range of this statistic for the LW fluxes suggests high confidence in our calculated radiative fluxes, which is maintained by the small σ values. However, the calculated surface SW_{dn} and TOA SW_{up} fluxes at the NSA site have a relatively large σ value, which can also be seen clearly in Figure 6k, and small sample number; the combination of these two results in a 90% confidence interval range of more than 130% and 80%, respectively. Depending on the site and flux type (TOA SW/LW_{up} and surface SW/LW_{dn}), the 90% confidence intervals contain anywhere between ~10 and 75% of the individual case values. The large standard deviations, which can be caused by a skewed distribution of solar zenith angles (or Julian day), are believed to limit the number of cases contained within the interval range. The Student's *t* distribution is only appropriate for normally distributed data, which is not necessarily applicable for all sites/cases here. Based on the flux comparisons in Figures 5 and 6, as well as in Tables 4 and 5, we can conclude that the input of accurate atmospheric profiles in the RTM plays an important role in calculating the surface and TOA SW and LW fluxes and that some surface characteristics must be adjusted to achieve radiative closure.

4. Conclusions

This study focuses on the evaluation of MERRA-2 clear-sky vertical profiles of temperature, ozone mixing ratio, and water vapor mixing ratio at three ARM sites (SGP, NSA, and TWPC3) from August 2004 to December 2013. Furthermore, the meteorological profiles are used as input to the NASA Langley-modified Fu-Liou RTM to perform a clear-sky radiation closure study for both the surface and TOA radiative fluxes. Based on the results presented in the preceding sections, the following conclusions can be made.

1. Vertical profiles of temperature at the three sites are well replicated in MERRA-2 when compared to the newly generated satellite/surface-based (hybrid) data set. Even the characteristic low-level temperature inversion of the Arctic is captured in the reanalysis. Since MLS ozone is directly assimilated, the MERRA-2 ozone mixing ratios are very close to the hybrid profiles at all three ARM sites. Finally, the MERRA-2 tropospheric water vapor mixing ratios are, on average, on the drier side of the combined satellite/surface-based data set at SGP and NSA for snow-free conditions. However, the relatively small and constant tropospheric water vapor profile at NSA for the snow cases is well replicated in MERRA-2. At TWPC3, the MERRA-2 water vapor profile is drier than the ARM-merged sounding by ~10–30%, on average, except between ~850 and 750 hPa.
2. The clear-sky surface and TOA radiative fluxes are calculated using the NASA Langley-modified RTM (with the same surface characteristics) with inputs from hybrid, MERRA-2, and climate mean profiles at three ARM sites. In this radiative closure study, calculated SW fluxes are tuned based upon adjustments to the surface albedo, and a secondary aerosol is included in order to reduce the differences between the averaged calculated and observed fluxes. As expected, the surface and TOA LW fluxes show little-to-no influence on the surface albedo and aerosol characteristics; therefore, some other method of adjustment is necessary for achieving radiative closure for these fluxes. We suggest tuning the surface skin temperature as a means for reducing the difference between the calculated and observed LW fluxes. The averaged flux differences (calculated minus observations) using the hybrid and MERRA-2 profiles at three ARM sites are generally below 5 W/m², while the calculated fluxes from climate mean profiles are typically higher biased. Although the averaged tuned calculated fluxes are relatively close to the observed means, large compensating errors are evident. Therefore, we can conclude that the input of accurate atmospheric profiles and surface characteristics in the RTM plays an important role in calculating the surface and TOA clear-sky SW and LW fluxes.

Appendix A: The Clear-Sky Case Days and Times (in UTC) for the Three ARM Sites

	Year	Julian Day	UTC Time		Year	Julian Day	UTC Time
SGP	2004	269	08:37	TWPC3	2007	059	22:33
	2004	349	08:36		2007	161	13:50
	2005	015	08:35		2007	168	13:56
	2005	022	19:45		2008	007	22:24
	2005	102	19:44		2008	039	22:23
	2005	134	19:44		2008	059	13:52
	2005	159	08:35		2008	347	13:51
	2005	175	08:34		2009	020	13:59
	2005	191	08:34		2009	080	22:30
	2005	287	08:35		2006	244	16:55
	2005	335	08:35		2006	245	05:10
	2005	342	19:45		2007	200	05:09
	2006	057	19:45		2007	248	05:09
	2006	178	08:37		2007	264	05:09
	2006	201	19:48		2007	280	05:09
	2006	242	08:39		2008	194	05:09
	2006	290	08:39		2008	209	16:54
	2006	338	08:38		2008	210	05:09
	2006	345	19:48		2009	163	16:57
	2007	28	19:48		2009	164	05:12
	2007	220	19:48		2009	195	16:57
	2007	293	08:38		2009	196	05:12
	2007	300	19:48				
	2007	364	19:46				
	2008	015	19:46				
	2008	040	08:35				
	2008	159	08:37				
	2008	207	08:38				
	2008	303	08:40				
	2009	001	08:40				
	2009	008	19:50				
	2009	033	08:41				
	2009	040	19:51				
	2009	049	08:42				
	2010	212	08:38				
	2011	007	08:37				
	2011	199	08:37				
	2011	263	08:36				
	2011	327	08:37				
	2011	359	08:37				
	2012	017	19:46				
	2012	065	19:47				
	2012	074	08:37				
	2012	138	08:37				
	2012	170	08:37				
	2012	177	19:47				
	2012	186	08:37				
	2012	202	08:37				
	2012	289	19:46				
	2013	019	19:47				
	2013	028	08:37				
NSA	2005	078	22:23				
	2005	146	13:52				
	2005	206	22:22				
	2006	168	22:31				
	2006	190	13:49				
	2007	036	22:27				
	2007	040	13:57				
	2007	043	22:33				

Acknowledgments

This work was supported by the NASA Earth and Space Science Fellowship program to Erica Dolinar at the University of North Dakota, under the advisement of Xiquan Dong. The researchers at UND were supported by NASA CERES project under grant NNX14AP84G and NOAA MAPP grant under NA13OAR4310105 at the University of North Dakota. Coauthor Jonathan Jiang acknowledges the support by the Jet Propulsion Laboratory, California Institute of Technology, under contract with NASA. We would also like to thank Norman Loeb for hosting Dolinar for a 13 week internship at NASA Langley Research Center and Science Systems and Applications Inc. for providing additional support. CERES SSF product is produced by the NASA CERES Team, available at <http://ceres.larc.nasa.gov>. The ground-based observations were obtained from the Atmospheric Radiation Measurement (ARM) Program sponsored by the U.S. Department of Energy (DOE) Office of Energy Research, Office of Health and Environmental Research, and Environmental Sciences Division. The ARM-merged soundings are downloaded from <http://www.archive.arm.gov/>. The MLS data are made available at <http://mls.jpl.nasa.gov/>.

References

- Alexandrov, M., B. Cairns, B. E. Carlson, and A. A. Lacis (2005), Fine and coarse mode aerosols in Southern Great Plains multi-filter rotating shadowband radiometer datasets Fifteenth ARM Science Team Meeting Proceedings, Daytona Beach, Fla., March 14–18.
- Allen, R. P. (2000), Evaluation of simulated clear-sky longwave radiation using ground-based observations, *J. Clim.*, *13*, 1951–1964.
- Bloom, S., et al. (2005), Documentation and validation of the Goddard Earth Observing System (GEOS) data assimilation system—version 4, NASA Technical Report Series on Global Modeling and Data Assimilation, NASA/TM-2005-104606, vol. 26, 165 pp. [Available at http://ntrs.nasa.gov/archive/nasa/casi.ntrs.nasa.gov/20050175690_2005173043.pdf].
- Bosilovich, M., et al. (2015), MERRA-2: Initial evaluation of the climate Technical Report Series on Global Modeling and Data Assimilation, NASA/TM-2015-104606/Vol.43.
- Brandt, R. E., S. G. Warren, A. P. Worby, and T. C. Grenfell (2005), Surface albedo of the Antarctic sea ice zone, *J. Clim.*, *18*, 3606–3622.
- Charlock, T. P., and T. L. Alberta (1996), The CERES/ARM/GEWEX Experiment (CAGEX) for the retrieval of radiative fluxes with satellite data, *Bull. Am. Meteorol. Soc.*, *77*(11), 2673–2683.
- Clothiaux, E. E., T. P. Ackerman, G. G. Mace, K. P. Moran, R. T. Marchand, M. A. Miller, and B. E. Martner (2000), Objective determination of cloud heights and radar reflectivities using a combination of active remote sensors at the Atmospheric Radiation Measurement Program Cloud and Radiation Test Bed (ARM CART) sites, *J. Appl. Meteorol.*, *39*, 645–665.
- Divakarla, M., et al. (2008), Evaluation of Atmospheric Infrared Sounder ozone profiles and total ozone retrievals with matched ozonesonde measurements, ECMWF ozone data, and Ozone Monitoring Instrument retrievals, *J. Geophys. Res.*, *113*, D15308, doi:10.1029/2007JD009317.
- Dolinar, E. K., X. Dong, B. Xi, J. H. Jiang, and H. Su (2015), Evaluation of CMIP5 simulated clouds and TOA radiation budgets using NASA satellite observations, *Clim. Dyn.*, *44*, 2229–2247, doi:10.1007/s00382-014-2158-9.
- Dong, X., B. Xi, and P. Minnis (2006), A climatology of midlatitude continental clouds from the ARM SGP central facility. Part II: Cloud Fraction and surface radiative forcing, *J. Clim.*, *19*, 1765–1783.
- Dong, X., B. Xi, K. Crosby, C. N. Long, R. S. Stone, and M. D. Shupe (2010), A 10 year climatology of Arctic cloud fraction and radiative forcing at Barrow, Alaska, *J. Geophys. Res.*, *115*, D17212, doi:10.1029/2009JD013489.
- Dong, X., B. Xi, S. Qiu, P. Minnis, S. Sun-Mack, and F. Rose (2016), A radiation closure study of Arctic cloud microphysical properties using the collocated satellite-surface data and Fu-Liou radiative transfer model, *J. Geophys. Res. Atmos.*, *121*, 10,175–10,198, doi:10.1002/2016JD025255.
- Dudek, M. P., X.-Z. Liang, and W.-C. Wang (1996), A regional climate model study of the scale dependence of cloud-radiation interactions, *J. Clim.*, *9*, 1221–1234, doi:10.1175/1520-0442(1996)09<1221:ARCMO>2.0.CO;2.
- Froidevaux, L., et al. (2008), Validation of Aura Microwave Limb Sounder stratospheric ozone measurements, *J. Geophys. Res.*, *113*, D15520, doi:10.1029/2007JD008771.
- Fu, Q., and K. N. Liou (1993), Parameterization of the radiative properties of cirrus clouds, *J. Atmos. Sci.*, *50*, 2008–2025, doi:10.1175/1520-0469(1993)050<2008:POTRPO>2.0.CO;2.
- Geier, E. B., R. N. Green, D. P. Kratz, P. Minnis, W. F. Miller, S. K. Nolan, and C. B. Franklin (2001), *Single Satellite Footprint TOA/Surface Fluxes and Clouds (SSF) Collection Document*, NASA Langley Res. Cent., Hampton, Va. [Available at http://asd-www.larc.nasa.gov/ceres/collect_guide/SSF.CG.pdf].
- Hartmann, D. L., V. Ramanathan, A. Berroir, and G. E. Hunt (1986), Earth Radiation Budget data and climate research, *Rev. Geophys.*, *24*(2), 439–468, doi:10.1029/RG024i002p00439.
- Hwang, Y.-T., D. M. W. Frierson, and J. E. Kay (2011), Coupling between Arctic feedbacks and changes in poleward energy transport, *Geophys. Res. Lett.*, *38*, L17704, doi:10.1029/2011GL048546.
- Jiang, J. H., et al. (2012), Evaluation of cloud and water vapor simulations in CMIP5 climate models using NASA A-Train satellite observations, *J. Geophys. Res.*, *117*, D14105, doi:10.1029/2011JD017237.
- Jiang, J. H., H. Su, C. Zhai, L. Wu, K. Minschwaner, A. M. Molod, and A. M. Tompkins (2015), An assessment of upper-troposphere and lower-stratosphere water vapor in MERRA, MERRA2 and ECMWF reanalyses using Aura MLS observations, *J. Geophys. Res. Atmos.*, *120*, 11,468–11,485, doi:10.1002/2015JD023752.
- Kato, S., F. G. Rose, and T. P. Charlock (2005), Computation of domain averaged irradiance using satellite-derived cloud properties, *J. Atmos. Oceanic Technol.*, *22*, 146–164.
- Khain, A., M. Ovtchinnikov, M. Pinsky, A. Pokrovsky, and H. Krugliak (2000), Notes on the state-of-the-art numerical modeling of cloud microphysics, *Atmos. Res.*, *55*, 159–224.
- Kiehl, J. T., and K. E. Trenberth (1997), Earth's annual global mean energy budget, *Bull. Am. Meteorol. Soc.*, *78*, 197–208, doi:10.1175/1520-0477(1997)078<0197:EAGMEB>2.0.CO;2.
- L'Ecuier, T. S., and J. H. Jiang (2010), Touring the atmosphere aboard the A-Train, *Phys. Today*, *63*(7), 36–41, doi:10.1063/1.3463626.
- Li, Z., M. C. Cribb, and A. P. Trishchenko (2002), Impact of surface inhomogeneity on solar radiative transfer under overcast conditions, *J. Geophys. Res.*, *107*(D16), 4294, doi:10.1029/2001JD000976.
- Livesey, N. J., et al. (2015), Version 4.2x level 2 data quality and description document Tech. Rep. JPL D-33509, Jet Propul. Lab., Calif. Inst. Of Technol., Pasadena, Calif.
- Loeb, N. G., S. Kato, N. Manalo-Smith, S. K. Gupta, W. F. Miller, P. Minnis, and B. A. Wielicki (2003), Angular distribution models for top-of-atmosphere radiative flux estimation from the Clouds and the Earth's Radiant Energy System instrument on the Tropical Rainfall Measuring Mission satellite. Part I: Methodology, *J. Appl. Meteorol.*, *42*, 240–26.
- Loeb, N. G., W. Sun, W. F. Miller, K. Loukachine, and R. Davies (2006), Fusion of CERES, MISR, and MODIS measurements for top-of-atmosphere radiative flux validation, *J. Geophys. Res.*, *111*, D18209, doi:10.1029/2006JD007146.
- Long, C. N., and D. D. Turner (2008), A method for continuous estimation of clear-sky downwelling longwave radiative flux developed using ARM surface measurements, *J. Geophys. Res.*, *113*, D18206, doi:10.1029/2008JD009936.
- Long, C. N., and Y. Shi (2008), An automated quality assessment and control algorithm for surface radiation measurements, *J. Open Atmos. Sci.*, *2*, 23–37.
- Menon, S., A. D. Del Genio, D. Koch, and G. Tselioudis (2002), GCM simulations of the aerosol indirect effect: Sensitivity to cloud parameterization and aerosol burden, *J. Atmos. Sci.*, *59*, 692–713, doi:10.1175/1520-0469(2002)059<0692:GSOTAI>2.0.CO;2.
- Molod, A., L. Takacs, M. Suarez, and J. Bacmeister (2015), Development of the GEOS-5 atmospheric general circulation model: Evolution from MERRA to MERRA2, *Geosci. Model Dev.*, *8*, 1339–1356, doi:10.5194/gmd-8-1339-2015.
- Moran, K. P., B. E. Martner, M. J. Post, R. A. Kropfli, D. C. Welsh, and K. B. Widener (1998), An unattended cloud-profiling radar for use in climate research, *Bull. Am. Meteorol. Soc.*, *79*, 443–455.

- Morris, V. R. (2006), Infrared thermometer (IRT) handbook DOE/SC-ARM TR-015.
- Moy, L. A., R. O. Knuteson, D. C. Tobin, H. E. Revercomb, L. A. Borg, and J. Susskind (2010), Comparison of measured and modeled outgoing longwave radiation for clear-sky ocean and land scenes using coincident CERES and AIRS observations, *J. Geophys. Res.*, *115*, D15110, doi:10.1029/2009JD012758.
- Pincus, R., C. P. Batstone, R. J. P. Hofmann, K. E. Taylor, and P. J. Glecker (2009), Evaluating the present-day simulation of clouds, precipitation, and radiation in climate models, *J. Geophys. Res.*, *113*, D14209, doi:10.1029/2007JD009334.
- Qin, Y., and R. M. Mitchell (2009), Characterisation of episodic aerosol types over the Australian continent, *Atmos. Chem. Phys.*, *9*, 1943–1956.
- Quinn, P. K., T. L. Miller, T. S. Bates, J. A. Ogren, E. Andrews, and G. E. Shaw (2002), A 3-year record of simultaneously measured aerosol chemical and optical properties at Barrow, Alaska, *J. Geophys. Res.*, *107*(D11), 4130, doi:10.1029/2001JD001248.
- Read, W. G., et al. (2007), Aura Microwave Limb Sounder upper tropospheric and lower stratospheric H₂O and RHi validation, *J. Geophys. Res.*, doi:10.1029/2007JD008752.
- Ramanathan, V. (1987), The role of Earth radiation budgets studies in climate and general circulation research, *J. Geophys. Res.*, *92*, 4075–4095, doi:10.1029/JD092iD04p04075.
- Ramanathan, V., R. D. Cess, E. F. Harrison, P. Minnis, B. R. Barkstrom, E. Ahmad, and D. Hartmann (1989), Cloud-radiative forcing and climate: Results from the Earth radiation budget experiment, *Science*, *243*, 57–63.
- Reichle, R. H., and Q. Liu (2014), Observation-corrected precipitation estimates in GEOS-5, NASA/TM-2014-104606, vol.35. [Available at <http://gmao.gsfc.nasa.gov/pubs/tm/docs/Reichle734.pdf>.]
- Ruzmaikin, A., H. H. Aumann, and J. H. Jiang (2015), Interhemispheric variability of the Earth's radiation, *J. Atmos. Sci.*, *72*(12), 4615–4628, doi:10.1175/JAS-D-15-0106.1.
- Schwartz, M. J., et al. (2008), Validation of the Aura Microwave Limb Sounder temperature and geopotential height measurements, *J. Geophys. Res.*, *113*, D15511, doi:10.1029/2007JD008783.
- Stackhouse, P. W., Jr., S. K. Gupta, S. J. Cox, T. Zhang, J. C. Mikovitz, and L. M. Hinkelman (2011), The NASA/GEWEX surface radiation budget release 3.0: 24.5-year dataset, *GEWEX News*, *21*(1), 10–12.
- Stanfield, R. E., X. Dong, B. Xi, A. D. Del Genio, P. Minnis, D. Doelling, and N. Loeb (2015), Assessment of NASA GISS CMIP5 and post-CMIP5 simulated clouds and TOA radiation budgets using satellite observations. Part II: TOA radiation budget and CREs, *J. Clim.*, *28*, doi:10.1175/JCLI-D-14-00249.1.
- Su, W., J. Corbett, Z. Eitzen, and L. Liang (2015a), Next-generation angular distribution models for top-of-atmosphere radiative flux calculation from CERES instruments: Methodology, *Atmos. Meas. Tech.*, *8*(2), 611–632, doi:10.5194/amt-8-611-2015.
- Su, W., J. Corbett, Z. Eitzen, and L. Liang (2015b), Next-generation angular distribution models for top-of-atmosphere radiative flux calculation from CERES instruments: Validation, *Atmos. Meas. Tech.*, *8*(8), 3297–3313, doi:10.5194/amt-8-3297-2015.
- Susskind, J., G. Molnar, L. Iredell, and N. G. Loeb (2012), Interannual variability of outgoing longwave radiation as observed by AIRS and CERES, *J. Geophys. Res.*, *117*, D23107, doi:10.1029/2012JD017997.
- Takacs, L. L., M. J. Suárez, and R. Todling (2016), Maintaining atmospheric mass and water balance in reanalyses, *Q. J. R. Meteorol. Soc.*, *142*, 1565–1573, doi:10.1002/qj.2763.
- Tegtmeier, S., et al. (2013), SPARC data initiative: A comparison of ozone climatologies from international satellite limb sounders, *J. Geophys. Res. Atmos.*, *118*, 12,229–12,247, doi:10.1002/2013JD019877.
- Tian, B., E. Manning, E. Fetzer, E. Olsen, and S. Wong (2014), AIRS version 6 L3 user guide AIRS/AMSU/HSB Version 6 Level 3 Product User Guide, Pasadena, Calif.
- Trenberth, K. E., J. T. Fasullo, and J. Kiehl (2009), Earth's global energy budget, *Bull. Am. Meteorol. Soc.*, *90*, 311–323, doi:10.1175/2008BAMS2634.1.
- Troyan, D. (2012), Merged sounding value-added product technical report U.S. Department of Energy. DOE/SC-ARM-TR-087.
- Waters, J., et al. (2006), The Earth Observing System Microwave Limb Sounder (EOS MLS) on the Aura satellite, *IEEE Trans. Geosci. Remote Sens.*, *44*(5), 1075–1092, doi:10.1109/TGRS.2006.873771.
- Wielicki, B. A., B. R. Barkstrom, E. F. Harrison, R. B. Lee, G. Louis Smith, and J. E. Cooper (1996), Clouds and the Earth's Radiant Energy System (CERES): An Earth Observing System experiment, *Bull. Am. Meteorol. Soc.*, *77*(5), 853–868.
- Wild, M., C. N. Long, and A. Uhmura (2006), Evaluation of clear-sky solar fluxes in GCMs participating in AMIP and IPCC-AR4 from a surface perspective, *J. Geophys. Res.*, *111*, D01104, doi:10.1029/2005JD006118.
- Wild, M., D. Folini, M. Z. Hakuba, C. Schär, S. I. Seneviratne, S. Kato, D. Rutan, C. Ammann, E. F. Wood, and G. König-Langlo (2015), The energy balance over land and oceans: An assessment based on direct observations and CMIP5 climate models, *Clim. Dyn.*, *44*(11–12), 3393–3429, doi:10.1007/s00382-014-2430-z.
- Zhang, Y.-C., W. B. Rossow, A. A. Lacis, M. I. Mishchenko, and V. Oinas (2004), Calculation of radiative fluxes from the surface to top-of-atmosphere based on ISCCP and other global datasets: Refinements of the radiative transfer model and the input data, *J. Geophys. Res.*, *109*, D19105, doi:10.1029/2003JD004457.